SLITRK6 mutations cause myopia and deafness in humans and mice

Mustafa Tekin,[1,2] Barry A. Chioza,[3] Yoshifumi Matsumoto,[4] Oscar Diaz-Horta,[1] Harold E. Cross,[5] Duygu Duman,[2] Haris Kokotas,[6] Heather L. Moore-Barton,[7] Kazuto Sakoori,[4] Maya Ota,[4] Yuri S. Odaka,[4] Joseph Foster II,[1] F. Basak Cengiz,[2] Suna Tokgoz-Yilmaz,[2] Oya Tekeli,[8] Maria Grigoriadou,[6] Michael B. Petersen,[6,9] Ajith Sreekantan-Nair,[3] Kay Gurtz,[10] Xia-Juan Xia,[11] Arti Pandya,[11] Michael A. Patton,[3] Juan I. Young,[1] Jun Aruga,[4] and Andrew H. Crosby[3]

[1]John P. Hussman Institute for Human Genomics and Dr. John T. Macdonald Department of Human Genetics, University of Miami Miller School of Medicine, Miami, Florida, USA. [2]Division of Pediatric Genetics, Ankara University School of Medicine, Ankara, Turkey. [3]Centre for Human Genetics, St. George's University of London, London, United Kingdom. [4]Laboratory for Behavioral and Developmental Disorders, RIKEN Brain Science Institute, Saitama, Japan. [5]Department of Ophthalmology, University of Arizona School of Medicine, Tucson, Arizona, USA. [6]Department of Genetics, Institute of Child Health, 'Aghia Sophia' Children's Hospital, Athens, Greece. [7]South West Thames Regional Genetics Services, St. George's University London, London, United Kingdom. [8]Department of Ophthalmology, Ankara University School of Medicine, Ankara, Turkey. [9]Department of Clinical Genetics, Aalborg Hospital, Aalborg, Denmark. [10]Windows of Hope Genetic Study, Geauga County, Ohio, USA. [11]Department of Human and Molecular Genetics, Virginia Commonwealth University, Richmond, Virginia, USA.

Myopia is by far the most common human eye disorder that is known to have a clear, albeit poorly defined, heritable component. In this study, we describe an autosomal-recessive syndrome characterized by high myopia and sensorineural deafness. Our molecular investigation in 3 families led to the identification of 3 homozygous nonsense mutations (p.R181X, p.S297X, and p.Q414X) in SLIT and NTRK-like family, member 6 (*SLITRK6*), a leucine-rich repeat domain transmembrane protein. All 3 mutant SLITRK6 proteins displayed defective cell surface localization. High-resolution MRI of WT and *Slitrk6*-deficient mouse eyes revealed axial length increase in the mutant (the endophenotype of myopia). Additionally, mutant mice exhibited auditory function deficits that mirrored the human phenotype. Histological investigation of WT and *Slitrk6*-deficient mouse retinas in postnatal development indicated a delay in synaptogenesis in *Slitrk6*-deficient animals. Taken together, our results showed that SLITRK6 plays a crucial role in the development of normal hearing as well as vision in humans and in mice and that its disruption leads to a syndrome characterized by severe myopia and deafness.

Introduction

Myopia is the most common cause of visual impairment worldwide (1). It affects more than 25% of adults in Western Europe and America, and its prevalence exceeds 70% in some urban areas of East Asia (2–4). High myopia, defined as refractive error greater than –6 or more diopters, affects approximately 1%–3% of the population (5) and is a significant risk factor for ocular comorbidity, including retinal detachment, macular degeneration, premature cataract, and glaucoma (1, 6). Data from several study types suggest a strong genetic component to myopia. The odds of a child becoming myopic rise with the number of myopic parents (7), and even the nonmyopic offspring of myopic parents have been shown to have longer eyes than nonmyopic children of nonmyopic parents (8). Twin studies add further support, indicating heritability values between 0.5 and 0.90 (9–11). Genome-wide association studies have identified putative gene loci on chromosomes 13q (12) and 15q (13, 14), as well as genetic variants in *CTNND2*, as being associated with myopia (15). Recently, a missense variant in *LEPREL1* (encoding prolyl 3-hydroxylase 2 [P3H2]), a 2-oxoglutarate–dependent dioxygenase that hydroxylates collagen molecules, was associated with an autosomal-recessive form of high myopia and early-onset cataracts in an Israeli-Bedouin kindred (16). However, although the magnitude of heritable factors in ocular refraction has been convincingly established, few association studies have been replicated in independent studies or candidate genes validated in inherited human conditions involving myopia (1). Consequently, the genes and molecular mechanisms important for normal human refractive development remain to be discovered.

Hearing loss is another common sensory disorder, with a prevalence of 1 in 1,000 at birth that almost doubles by 9 years of age (6, 17). Although the incidence of hearing loss in individuals with myopia is unknown, the prevalence of ocular abnormalities in deaf children is high (17). It is known that greater than 50% of permanent childhood hearing impairment in the developed world has a genetic etiology (6), and many syndromic forms of hearing loss have been described. Nonsyndromic hearing loss is similarly genetically heterogeneous, with greater than 150 loci and greater than 40 genes identified (6).

More than 150 genetic syndromes are associated with high myopia and more than 400 with hearing loss (OMIM). Several syndromes have previously been described that involve myopia as well as deafness, although all involve abnormalities in other systems or involve other ocular abnormalities. A well-known example is Stickler syndrome (OMIM 108300), in which patients present with midfacial underdevelopment, cleft palate, spondyloepiphyseal dysplasia, and/or precocious arthritis in addition to hearing loss and myopia (18). Mutations in genes encoding various collagen proteins (COL2A1, COL9A1, COL9A2, COL11A1, or COL11A2) cause Stickler syndrome (18). In Donnai-Barrow syndrome (OMIM 222448), a rare disorder also involving hearing loss and myopia due to mutations in lipoprotein receptor–related protein 2 precursor

---

Authorship note: Barry A. Chioza, Yoshifumi Matsumoto, and Oscar Diaz-Horta contributed equally to this work.

Conflict of interest: The authors have declared that no conflict of interest exists.

Citation for this article: *J Clin Invest.* 2013;123(5):2094–2102. doi:10.1172/JCI65853.

Table 1

Clinical overview of patients

Patient (current age)	Myopia		Sensorineural hearing loss	
	Age at diagnosis	Current severity[A]	Age at diagnosis	Current severity[B]
Family 1 (Amish)				
XI:2 (14 yr)	1 yr	–7.25	Congenital[C]	Severe
XI:3 (13 yr)	1 yr	–9.75	2 yr	Moderate
XI:4 (9 yr)	1 yr	–10.50	2 yr	Severe
Family 2 (Turkish)				
IV:1 (60 yr)	Infancy	–8.25	Prelingual	Moderate
IV:2 (54 yr)	Early childhood	–6.25	Prelingual	Severe
IV:3 (52 yr)	Early childhood	–6	Prelingual	Profound
IV:6 (44 yr)	Infancy	–11	Prelingual	Profound
Family 3 (Greek)				
II:1 (young adult)	NA	NA	Prelingual	Severe
II:2 (young adult)	NA	NA	Prelingual	Severe

[A] Diopters in better eye. [B] Better ear. [C] Newborn screen.

(*LRP2*), affected individuals have ocular hypertelorism, enlarged fontanelle, agenesis of the corpus callosum, intellectual disability, and congenital diaphragmatic hernia and/or omphalocele (19).

We describe here the first syndrome of severe congenital myopia and sensorineural hearing loss in the absence of other systemic, ocular, or connective tissue manifestations. Our findings demonstrated a major role of SLIT and NTRK-like family, member 6 (SLITRK6), in the molecular pathways important for normal human and mouse vision and hearing and shed light on biological processes that may be perturbed and subsequently result in high myopia and deafness.

Results

SLITRK6 mutations cause high myopia and sensorineural deafness in humans. We initially observed a previously unrecognized syndrome characterized by high myopia and deafness in 2 families: family 1 was an old-order Amish family with autosomal-recessive congenital myopia and prelingual sensorineural hearing loss (Table 1, Figure 1A, and Supplemental Figure 1; supplemental material available online with this article; doi:10.1172/JCI65853DS1). 3 affected siblings have congenital high myopia (refraction error ranging from –7.25 to –10.5 diopters in affected individuals) corrected by glasses and prelingual-onset moderate to severe bilateral sensorineural hearing loss necessitating aids. The parents had low myopia (both –3.0 diopters) of youth onset with normal hearing. Family 2 was a consanguineous Turkish family with 4 affected individuals (Figure 1E). All affected individuals had high myopia (refraction error ranging from –6.0 to –11.0 diopters) and prelingual-onset moderate to profound sensorineural hearing loss. The parents and 2 unaffected siblings did not have hearing loss; the father and 2 unaffected siblings had adult-onset myopia (less than –2 diopters). Affected individuals in both families did not have delays in gross motor development; neither did they have balance problems, vertigo, dizziness, or spontaneous or positional nystagmus. Tandem walking was normal, and Romberg test was negative. CT scans of temporal bones were normal in 1 affected person in each family. Clinical examination confirmed the absence of additional findings, with normal facial appearance, neurological, connective tissue, and ocular manifestations. There was no retinitis pigmentosa in any affected subject.

To map the chromosomal location of the disease gene in family 1, a genome-wide SNP analysis was undertaken using samples from all affected family members (XI:2, XI:3, and XI:4; Figure 1A). This identified a single homozygous region shared among all affected individuals of 12.2 Mb of chromosome 13q31.1–13q31.3 (Figure 1B), delimited by recombinant SNP markers rs1333404 and rs9584101, likely to correspond to the disease locus. No other notable regions of autozygosity were observed. Autozygosity across this interval was corroborated by microsatellite marker analysis in all family members, which defined a haplotype that cosegregated with disease phenotype (Supplemental Figure 2).

The identified expanse of chromosome 13 corresponded to a particularly gene-poor region containing few coding sequences and putative functional transcripts. To identify the causative mutation, we sequenced all 5 protein-coding RefSeq (http://www.ncbi.nlm.nih.gov/RefSeq/) genes (*SLITRK1*, OMIM 609678; *SLITRK5*, OMIM 609680; *SLITRK6*, OMIM 609681; *GPC5*, OMIM 602446; the first exon of *GPC6*, OMIM 604404) as well as numerous microRNAs and other potentially functional molecules located within the disease interval (*LOC642345*; *MIR4500*; *MIR622*; *LOC144776*; *MIR17HG*, OMIM 609415; *MIR17*, OMIM 609416; *MIR18A*, OMIM 609417; *MIR19A*, OMIM 609418; *MIR20A*, OMIM 609420; *MIR19B1*, OMIM 609419; *MIR92A1*, OMIM 609422). This revealed a single novel sequence variant (NM_032229.2:c.1240C>T; NP_115605.2:p.Q414X; chromosomal variant NC_000013.10:g.86369404C>T; Figure 1D and Supplemental Figure 3) in exon 2 of *SLITRK6*. Sanger sequence analysis of all family members indicated that all affected children were homozygous for this variant, while the parents and unaffected sibling were all heterozygous. As the variant creates a PsiI restriction endonuclease recognition site, this finding was also confirmed by restriction digestion of PCR products encompassing this base change (Figure 1C). The variant was also detected in the RNA transcript via Sanger sequencing. It was not present in genomic databases (dbSNP135, http://www.ncbi.nlm.nih.gov/SNP/; 1,000 Genomes, http://www.1000genomes.org/) and was not detected in 450 control individuals of European ancestry; only a single heterozygous carrier individual was detected in the analysis of 80 Amish controls.

In parallel with the positional cloning effort in family 1, whole exome sequencing was performed in 2 affected individuals in family 2 (IV:2 and IV:6; Figure 1E) in order to identify the causative mutation. The exome sequencing experiment produced 74,112,314 and 83,126,193 reads for IV:2 and IV:6, respectively. When measured at a minimum depth of 8×, 89% of the target region was covered in both samples, with an average depth of 48× and 55× for IV:2 and IV:6, respectively. Likewise, when measured at 1× and 20× coverage, 98% and 62% (IV:2) and 98% and 69% (IV:6) of the intended target was covered, respectively. In terms of variant calls, the Burrows-Wheeler alignment (BWA) predicted the presence of 33,230 variants in both samples, either homozygous or heterozygous. By using our filtering tool (see Methods), only 1 shared homozygous variant at position ch13:86369754G>T (hg19) was detected, corresponding to c.890C>A (p.S297X) in *SLITRK6*

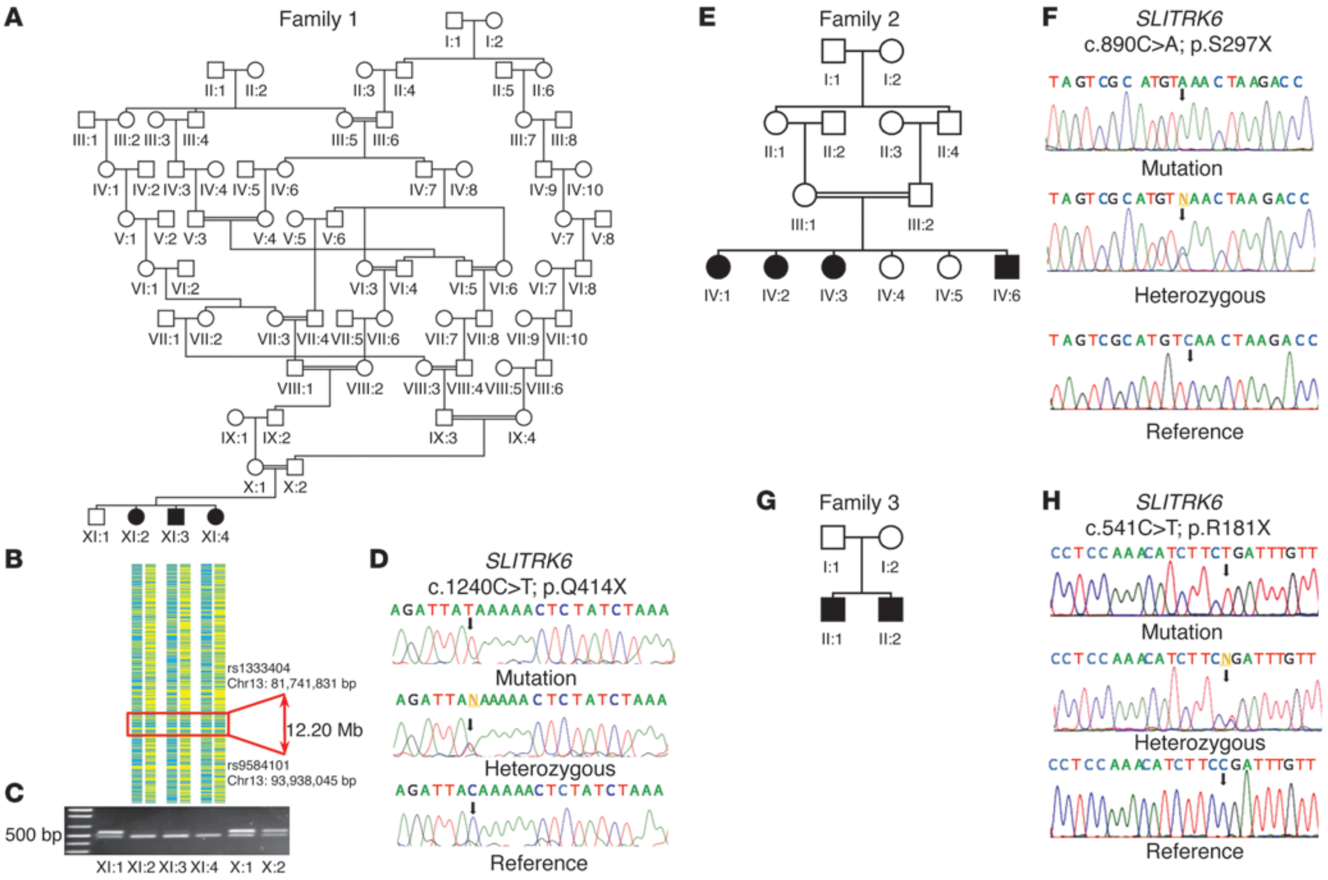

Figure 1

Families and identified *SLITRK6* mutations. (**A**–**D**) Family 1 (Amish). (**A**) Pedigree diagram. (**B**) Graphical representation of genotypes across chromosome 13. (**C**) PsiI restriction digestion of *SLITRK* exon 2 PCR product, confirming that all affected individuals were homozygous, and parents and unaffected sibling heterozygous, for the smaller digested 1240C>T *SLITRK6* allele. DNA marker is shown at far left; family members are as indicated. (**D**) Electropherograms showing the identified mutation. (**E** and **F**) Family 2 (Turkish). (**E**) Pedigree diagram. Individuals IV:1, IV:2, IV:3, and IV:6 were homozygous and IV:4, IV:5, III:1, and III:2 heterozygous for p.S297X. (**F**) Electropherograms showing the identified mutation. (**G** and **H**) Family 3 (Greek). (**G**) Pedigree diagram. Individuals II:1 and II:2 were homozygous and I:1 and I:2 heterozygous for p.R181X. (**H**) Electropherograms showing the identified mutation.

(Figure 1F). There were 62 and 66 sequence reads of the variant allele in IV:2 and IV:6, respectively, and 0 read of the reference. The identified variant was within a 10.3-MB homozygous run between 82,265,080 and 92,560,201 bps on chromosome 13. It was absent in the dbSNP135 and NHLBI Exome Sequencing Project databases (Exome Variant Server; http://evs.gs.washington.edu/EVS/). Sanger sequencing confirmed the variant and showed its cosegregation in the entire family and absence in 330 Turkish controls. To find additional mutations in *SLITRK6*, linkage to the *SLITRK6* locus was evaluated in 177 multiplex families with autosomal-recessive deafness. Affected individuals in these families had congenital or prelingual-onset severe to profound sensorineural hearing loss. Although myopia was present in some families, none was considered to have a syndromic form of deafness. When more than 2 affected members had the same haplotype flanking *SLITRK6*, Sanger sequencing of the entire gene was performed. This analysis revealed a Greek family with 2 affected children having a homozygous c.541C>T (p.R181X) mutation (family 3; Figure 1, G and H). Both parents were heterozygous for the mutation. This mutation was absent in 300 Greek controls. The p.R181X and p.S297X mutations were screened in 370 American probands with sensorineural hearing loss who are not known to have a syndrome. This study identified no sequence variants.

Detected SLITRK6 mutations do not cause mRNA decay. Since all 3 detected mutations in *SLITRK6* were nonsense, they might trigger the nonsense-mediated mRNA decay response, thereby leading to the absence of mRNA for translation into the SLITRK6 protein. Serial quantitative PCR measurements of mRNA levels of each mutant gene along with WT *SLITRK6* transfected into HEK293 cells showed comparable stability of each mRNA relative to the WT (Supplemental Figure 4), which suggests that none of the identified mutations triggers the nonsense-mediated mRNA response.

SLITRK6 mutations result in loss of function. *SLITRK6* belongs to the *SLITRK* family of genes, which encode single-pass (type 1) transmembrane proteins with 2 leucine-rich repeat (LRR) domains in the aminoterminal two-thirds of the molecule and a putative transmembrane domain located toward the carboxyterminal end (20, 21). Rodent SLITRK6 proteins are known to have synapse-inducing (22) and neurite-modulating (23) activity in cultured cells. We first studied the subcellular localization of WT human SLITRK6 and all

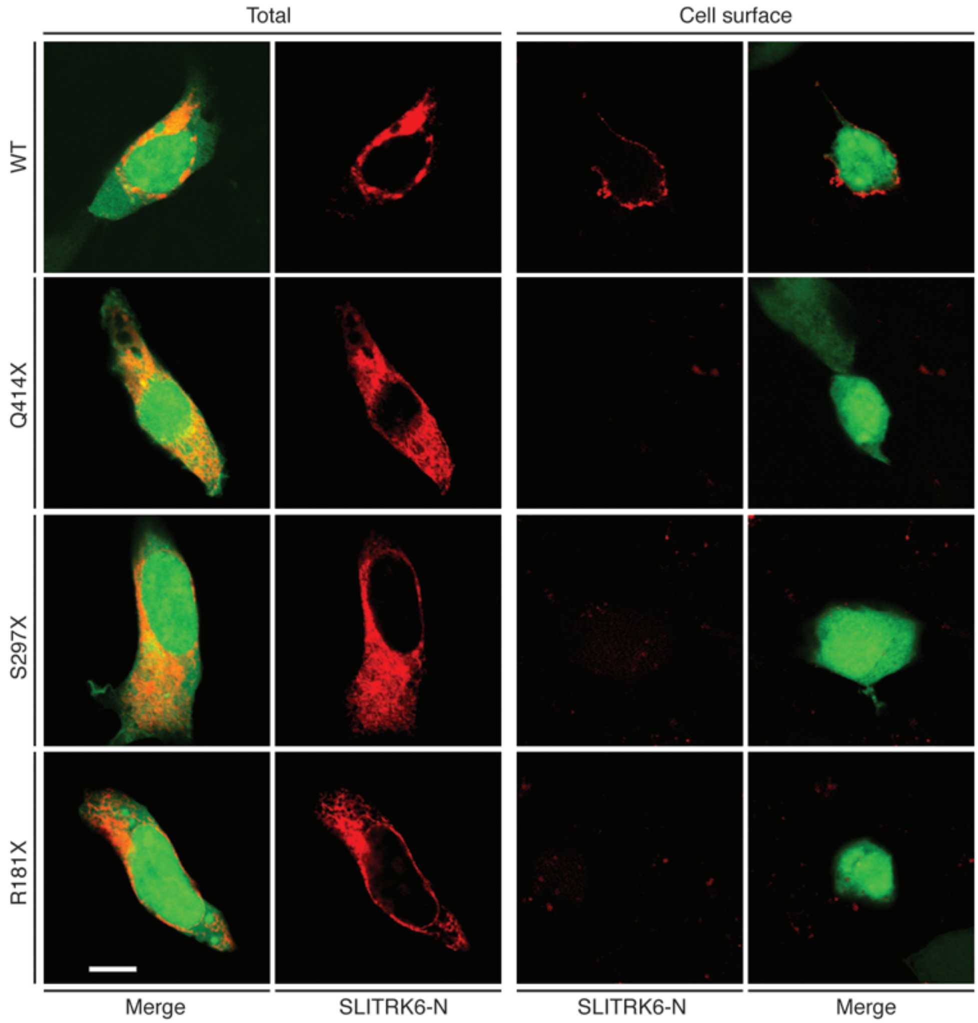

Figure 2
SLITRK6^{Q414X}, *SLITRK6*^{S297X}, and *SLITRK6*^{R181X} are defective in cell surface localization. WT *SLITRK6* and mutant *SLITRK6* expression vectors were transfected into HEK293 cells. Total and cell surface proteins in the transfectants were detected by antibody against the aminoterminus of SLITRK6 protein (red), whereas transfected cells were marked by GFP (green). Only WT SLITRK6 was detected at the cell surface. Scale bar: 10 μm.

3 mutations. We constructed CAG-*SLITRK6*-ires-EGFP expression vectors and transfected them into nonneural (HEK293) cells. WT *SLITRK6* and all 3 mutants were detected in immunostaining of the permeabilized cells using an antibody recognizing an aminoterminal epitope of SLITRK6 (Figure 2). However, in a nonpermeabilized condition, WT *SLITRK6*, but not the 3 mutants, gave immunopositive signals (Figure 2), which indicates that the mutations impaired cell surface expression. Accordingly, when the transfectants were cocultured with dissociated rat hippocampal neurons, synapse-inducing activity was observed in human WT *SLITRK6*, but not in the 3 *SLITRK6* variants (Supplemental Figure 5A). Furthermore, human WT *SLITRK6* reduced both neurite number and length of the PC12 cells treated with nerve growth factor (NGF) in a manner comparable to mouse *Slitrk6* (19), but the 3 variants did not show significant effects on the neurite properties (Supplemental Figure 5B). Taken together, these observations revealed dramatic effects of all 3 nonsense mutations on *SLITRK6* function and suggest that a null mechanism most likely relates to these mutations.

Mouse Slitrk6 KO presents with deafness and myopia. To verify the phenotypical consequence of the *SLITRK6* mutations obtained in humans, we undertook detailed phenotype analysis of *Slitrk6* KO (*Slitrk6*$^{-/-}$) mice. We previously showed that both male and female *Slitrk6* KO mice grow without showing any external abnormalities and are fertile (24). Our previous experiments showed that in the developing inner ear, *Slitrk6* KO mice have pronounced reduction of cochlear innervation, despite normal gross morphology and general organization of the organ of Corti (24). More recently, we demonstrated functional deficits in adult *Slitrk6* KO mice, which have reduced startle response and impaired auditory brainstem responses consistent with mid-frequency range hearing loss (25). This is consistent with the sensorineural hearing loss phenotype in human subjects with *SLITRK6* null mutations.

Since little is known about the eye phenotype of *Slitrk6* KO mice, we addressed the ocular manifestations in this study. We investigated 10- to 12-month-old *Slitrk6* KO and WT adult male mice using high-resolution small animal MRI scanning, as previously described (26). This revealed a significant increase in axial length (3.2%; $P = 0.017$), but not in lens thickness, of *Slitrk6* KO versus WT animals (Figure 3). This size difference in axial length was not apparent in newborn mice, as determined in serial sections of freshly frozen eyes (Figure 3), which indicates that SLITRK6 regulates eye growth after birth. It is known that axial length is the endophenotype of myopia in animal models, with greater length being associated with more severe myopia (27). Consequently, *Slitrk6* KO mice appear to closely mimic the human phenotype involving myopia, in association with the previously documented deafness.

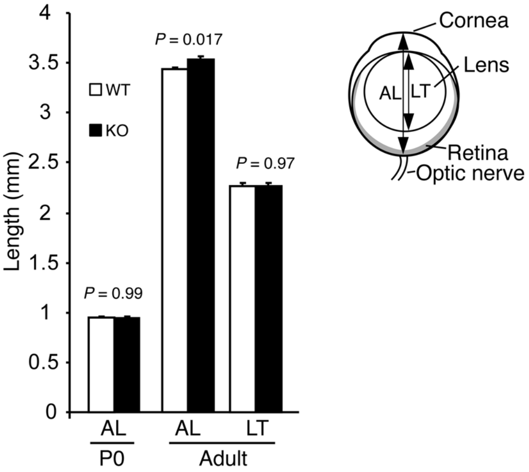

Figure 3
Increased axial length of the eyes of *Slitrk6* KO mice. Axial length (AL) and lens thickness (LT) were measured in male 10- to 12-month-old WT (n = 13) and *Slitrk6* KO (n = 10) adult mice using MRI. Measurements of newborn (P0) WT (n = 10) and *Slitrk6* KO (n = 10) mice were made using serial sections of rapidly frozen fresh eyes. For each animal, mean values of left and right eyes were first determined. Mean values were then used for statistical analysis for genotype-dependent differences. Bars indicate mean ± SEM. A significant difference between WT and *Slitrk6* KO mice was observed in adult axial length. P values are based on 2-tailed t test. Parameters used for the analysis are illustrated.

We next investigated the temporospatial expression pattern of SLITRK6 during development. In the newborn, *Slitrk6* mRNA was broadly detected in neural retina (Figure 4, A and B, and Supplemental Figure 6). Later, in P10 retina, expression was enhanced in the inner nuclear and outer plexiform layers (Figure 4, C, D, G, and H). Expression weakened as development proceeded, and *Slitrk6* mRNA was detected in the inner nuclear layer and in a subset of cells in the ganglion cell layer of adult mice (Figure 4, E and F). We next investigated the *Slitrk6* KO retina in postnatal development histologically. There were no overt abnormalities in gross layer organization in conventional histological staining (data not shown). However, when we examined the synapse markers Ribeye, Vglut1, and Vgat by immunofluorescence staining in *Slitrk6* KO retina, it became clear that the Ribeye signal in the outer plexiform layer was significantly lower than in WT retina (32%; P = 0.0031) — and Vglut1 in the outer plexiform layer and Vgat in the inner plexiform layer tended to be lower — at P10, when synaptogenesis was actively taking place (Figure 5, A and B, and Supplemental Figure 7). Ribeye expression was not detected at P7 in either *Slitrk6* KO or WT animals (Figure 5A) and was detected equally in adult animals (Supplemental Figure 8). In addition, anti-neurofilament staining for the retinal ganglion cell nerve fibers was reduced, albeit not significantly (Figure 5B and Supplemental Figure 7). Conversely, retinal cell type–specific markers (rhodopsin for rod photoreceptor cells, protein kinase C for bipolar cells, tyrosine hydroxylase for amacrine cells, Thy1 for retinal ganglion cells, and glutamine synthetase for Müller glia cells) did not show clear genotype-dependent changes during immunostaining (Supplemental Figure 7). Collectively, these results were indicative of delayed synaptogenesis in *Slitrk6* KO retina. To our knowledge, this is the first indication of the involvement of SLITRK6 in synaptogenesis in vivo. Ribeye is the marker for "ribbon synapse," which has been proposed to sustain high rates of exocytosis for relatively long periods (28). Interestingly, inner ear hair cells and retinal photoreceptor cells both possess this unique type of synapse, which indicates that SLITRK6 may play a similar role in retinal and inner ear development.

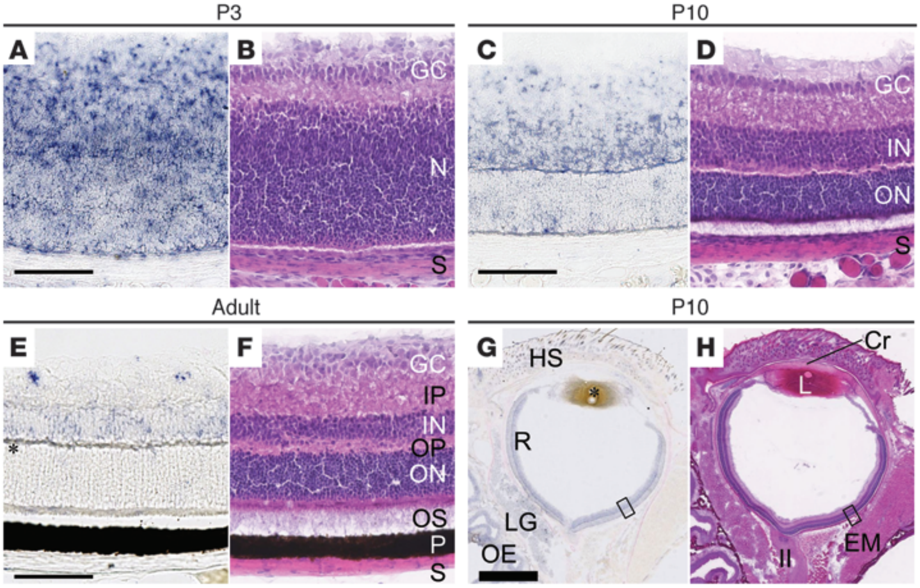

Figure 4
Postnatal *Slitrk6* expression in the murine eye. *Slitrk6* in situ hybridization (**A**, **C**, **E**, and **G**; purple stain) and hematoxylin and eosin staining (**B**, **D**, **F**, and **H**) in adjacent sections in P3, P10, and 11-week-old adult mice. (**A**–**F**) Retinal layers. (**G** and **H**) Horizontal sections through eye. (**A** and **B**) In the newborn, *Slitrk6* mRNA was broadly detected in neural retina. (**C** and **D**) At P10, expression became enhanced at the inner nuclear layer (IN), whereas moderate expression continued in the ganglion cell layer (GC). Images are higher-magnification views of boxed regions in **G** and **H**. (**E** and **F**) Expression weakened as development proceeded, and expression was detected at the inner nuclear layer and in a subset of cells in the ganglion cell layer in adult mice. (**G** and **H**) In the tissues surrounding the eye, weak expression was detected in the hair root sheath (HS), lacrimal gland (LG), and olfactory epithelium (OE) at P10. The gray line in the outer plexiform layer (OP) and the layer containing outer and inner segments of photoreceptor cells (OS) in adults (**E**, asterisk) and the brown staining in the lens (L) at P10 (**G**, asterisk) were not authentic in situ hybridization signals. Parallel lines in **H** denote optic nerve. Cr, cornea; EM, extraocular muscle; IP, inner plexiform layer; N, retinal neuroblastic layer; ON, outer nuclear layer; R, retina; S, sclera. Scale bars: 100 μm (**A**–**F**); 1 mm (**G** and **H**).

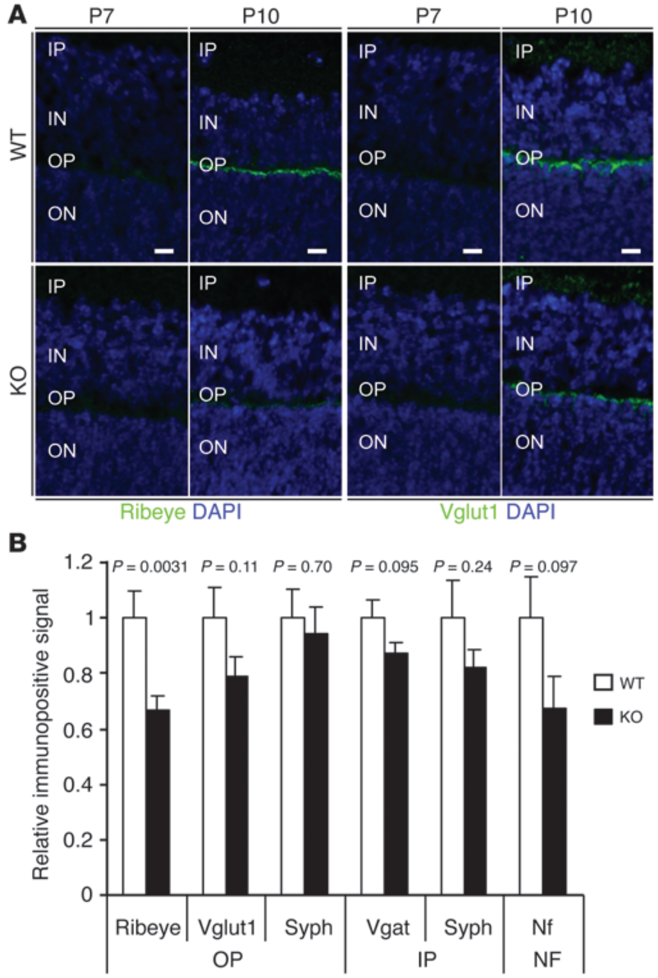

Figure 5

Analysis of the synapse markers Ribeye and Vglut1 in *Slitrk6* KO mice. (**A**) The ribbon synapse marker Ribeye and the glutamate-containing synaptic vesicle marker Vglut1 were examined in P7 and P10 mouse eyes by immunofluorescence staining. Layer abbreviations as in Figure 4. (**B**) Densitometric quantification of the immunopositive signals of immunostained images in **A** and Supplemental Figure 7. Shown are results for Ribeye, Vglut1, and the synaptic vesicle marker synaptophysin (Syph) in the outer plexiform layer; the GABA-containing synaptic vesicle marker Vgat and synaptophysin in the inner plexiform layer; and the neuronal marker neurofilament (Nf) in the nerve fiber layer (NF). Results are presented relative to WT levels (assigned as 1). *n* = 11–18 P10 retinas from independent animals for each genotype. *P* values are based on 2-tailed *t* test.

Discussion

Although various heritability measures, twin studies, and genetic analyses have indicated a strong genetic component in myopia, little remains known about the specific genetic and molecular basis of this common eye disorder. In the current study, we showed that mutation of *SLITRK6* results in a human syndrome that includes high myopia and sensorineural deafness as the only clinical findings and confirmed a similar phenotype in *Slitrk6* mutant mice. *SLITRK* gene family members are highly expressed in both human and murine central nervous systems (20, 21) and are currently considered emerging candidate genes for neuropsychiatric disorders (29). The family consist of 6 structurally related transmembrane proteins belonging to the LRR superfamily and are single-pass (type 1) transmembrane proteins highly expressed in the central nervous system (23). Among the mouse *Slitrk* family, *Slitrk6* has been shown to display strong expression in cochlea and retina in mouse embryos. Specifically, in the developing cochlea, SLITRK6 signals are evident in the primitive sensory neuroepithelium that gives rise to cochlear hair cells, and in the developing eye, expression is observed in the retinal outer neuroblastic layer, eyelid, and extraocular orbital mesenchymal tissue (21, 30).

Our present findings, along with previous studies investigating the role of SLITRK6 in inner ear development (24), suggest that SLITRK6 is involved in innervation of the developing murine eye and ear. We observed impaired synapse-inducing activity of *SLITRK6* mutants as well as delayed formation of synapses in the eyes of *Slitrk6* mutant mice. Vglut1 and Vgat, both markers of synaptic formation, were reduced in P10 retina of *Slitrk6* mutant mice, which indicates that SLITRK6 may possess the ability to recruit or induce the formation of Vglut1- and Vgat1-positive neuronal structures (22). Consequently, while a general delay in neuronal maturation cannot be ruled out, the pathogenetic mechanism underlying the eye and ear phenotype in this syndrome may involve impairment of neural circuit formation.

Myopia and other refractive-error disorders are consequences of uncoordinated development and contributions of a number of ocular components to overall eye structure, in particular axial length, which is generally accepted to be the main determinant of refractive error. By investigating *Slitrk6* KO mice, we showed that the myopia was likely due to increased axial eye length, a feature not previously recognized in these animals, which indicates a key role for SLITRK6 in this process. We detected no evidence for the occurrence of other eye disorders that typically accompany high myopia — such as cataract, glaucoma, and chorioretinal abnormalities — in either humans or mice; therefore, the *Slitrk6* KO mouse model represents a valuable tool for further investigation of the molecular and biological basis of the axial length endophenotype. Numerous lines of evidence support the existence of an active emmetropization mechanism, which controls the location of the retina by remodeling the sclera so that images can be focused on the focal plane (31–33). Alterations in axial elongation produced by the emmetropization mechanism may involve modulating normal postnatal growth, not ceasing or initiating growth, although much remains to be discovered. Interestingly, in embryonic mice, cochlear *Slitrk6* is thought to regulate expression of neurotrophic factors (24) that have been implicated in experience-dependent development of retinal function (34), which suggests a possible role for SLITRK6 in emmetropization via neurotrophin modulation.

Methods

Further information can be found in Supplemental Methods.

Sample preparation. DNA was extracted from blood via standard methods. 1 affected individual from each family was prescreened and found to be negative for common causes of nonsyndromic deafness, including mutations in *GJB2* (OMIM 121011), and for the m.A1555G mutation in *MTRNR1* (OMIM 561000). RNA was isolated from venous blood using the PAXgene method (QIAGEN), and cDNA synthesis from extracted RNA was undertaken with PrimeScript One Step RT-PCR Kit (version 2; TaKaRa).

Genotyping and autozygosity mapping. Autozygosity mapping was performed with Illumina Human Cyto12 beadchip arrays incorporating approximately 330,000 genetic markers in family 1. To screen additional families for linkage to the *SLITRK6* locus, rs431057, rs675302, rs2149266, and rs9531843 were genotyped with custom TaqMan probes in 177 multiplex families with autosomal-recessive deafness. For each TaqMan reaction, 10 ng DNA was mixed with TaqMan Universal PCR Master Mix (2×; Applied Biosystems) and SNP Genotyping Assay (20×). PCR conditions were 50°C for 2 minutes, 95°C for 10 minutes, 40 cycles of 95°C for 15 seconds, and 60°C for 1 minute. Data were analyzed with SDS 2.3 software (Applied Biosystems).

Whole exome sequencing. Genomic DNA from 2 affected individuals of family 2 were used to sequence the whole exomes, as previously described (35). The SureSelect Human All Exon 50 Mb kit (Agilent) was used for in-solution enrichment of coding exons and flanking intronic sequences following the manufacturer's standard protocol. Adapter sequences for the Illumina Hiseq2000 were ligated, and the enriched DNA samples were subjected to standard sample preparation for the Hiseq2000 instrument (Illumina). Paired-end reads of 99 bases in length were produced. The Illumina CASAVA version 1.8 pipeline was used to produce 99-bp sequence reads. BWA (36) was used to align sequence reads to the human reference genome (hg19), and variants were called using the GATK software package (37, 38). All variants were submitted to SeattleSeq134 (http://snp.gs.washington.edu/SeattleSeqAnnotation) for further characterization.

The Genomes Management Application (GEMapp) of University of Miami Miller School of Medicine (https://genomics.med.miami.edu/), was used to filter variants. The variants were filtered according to the inheritance model (autosomal-recessive with both homozygous and compound heterozygous), the variant function class including missense, nonsense, splice sites, in-frame and frame-shift indels, presence, and frequency at the dbSNP135 (http://www.ncbi.nlm.nih.gov/SNP/) and NHLBI (http://evs.gs.washington.edu/EVS/) databases (minor allele frequency of less than 1% was used). Variants were also filtered for the absence in more than 5 families samples in our internal database that includes more than 350 exomes. GATK quality score (QUAL) was set to 100 and genotype quality (GQ) to 50.

Sanger sequencing. Sanger sequencing was used to analyze RefSeq (www.ncbi.nlm.nih.gov/RefSeq/) genes as well as microRNA and other potentially functional molecules within the disease interval in family 1, to confirm the variant obtained through whole exome sequencing in family 2, to identify the variant in family 3, and to evaluate cosegregation in all families. PCR primers were designed using Primer3Plus software (http://www.bioinformatics.nl/cgi-bin/primer3plus/primer3plus.cgi) encompassing all coding exons and associated intron-exon splice boundaries (*SLITRK6* primers shown in Supplemental Table 1). PCR reactions were run in 25 μl volume, applying a touch-down protocol and annealing temperatures between 65°C and 57°C. We visualized PCR products on agarose gels, cleaned over Sephadex columns or with ExoSAP-IT (GE Healthcare), and applied to BigDye reactions following the manufacturer's recommendations (Applied Biosystems). A DNA Sequencer (ABI 3730) was used to detect the mutation. Sequences were analyzed using Mutation Surveyor software (version 3.20; SoftGenetics).

mRNA nonsense-mediated decay. Genomic DNA from patients homozygous for c.541C>T (p.R181X), c.890C>A (p.S297X), or c.1240C>T (p.Q414X) and from a control individual was amplified by high-fidelity PCR using primer pairs shown in Supplemental Table 1. The resulting 2 segments overlapping a unique EcoRI restriction site and comprising the 5′ untranslated region, intron, and coding exon of *SLITRK6* were subcloned into a pCR2.1-TOPO vector (Invitrogen). The inserts were removed with PacI-EcoRI and EcoRI-NotI and sequentially cloned downstream of the CMV promoter contained in an expression vector that also carries the EF-1α–EGFP expression cassette (pA1 vector; gift from Z. Zhou, University of Pennsylvania, Philadelphia, Pennsylvania, USA). HEK293 cells were transfected with pA1 vectors containing WT *SLITRK6* and mutant *SLITRK6* minigenes to investigate the stability of mRNA variants by quantitative real-time PCR using Sybr Green (Applied Biosystems) and primers shown in Supplemental Table 1 after treatment with actinomycin-D, an inhibitor of RNA synthesis.

SLITRK6 mRNA level was normalized with 18S rRNA, which is transcribed with an actinomycin-D–insensitive polymerase. Post-PCR Sanger sequencing confirmed correct splicing and transcription of mutant and WT *SLITRK6*.

SLITRK6 expression constructs. SLITRK6 protein coding regions were PCR amplified from genomic DNA of a healthy human subject or from cloned DNA of the patients using primers 5′-CCACCATGCCGCTGTGGATTCATC-3′ and 5′-CTATGTTTGCTGCTCCAGGAC-3′ and cloned into pGEMT easy plasmid vector (Promega). The resultant NotI fragments containing the entire protein coding region preceded by Kozak consensus sequence were inserted into pEF–ires–alkaline phosphatase expression vector (19) or pCAG-ires-EGFP vector (39).

Slitrk6 KO mice. *Slitrk6* null allele (*Slitrk6*$^{-}$) was generated by replacing its entire protein coding region by a loxP sequence (3). *Slitrk6* KO (*Slitrk6*$^{-/-}$) mice were generated using 129/Ola-derived ES cells and were backcrossed to C57BL/6J mice for more than 14 generations. Both male and female *Slitrk6* KO mice grew without showing any external abnormalities and were fertile (3).

MRI analysis. MRI analysis of adult mouse eyes was performed essentially as described previously (4). MRI images were acquired by subjecting anesthetized mice to MRI scan using a vertical bore 9.4-T Bruker AVANCE 400WB imaging spectrometer (Bruker BioSpin). Animals were anesthetized with intraperitoneal injection of ketamine (100 mg/kg) and xylazine (10 mg/kg) for induction, and 0.5% isoflurane in air (2 l/min flow rate) for maintenance. A contrasting agent (371 mg/ml meglumine gadopentetate; FujiPharma) was used as eyedrops to highlight the anterior chamber. MRI images were obtained using the FISP-3D protocol of Paravision software (version 5.0; Bruker BioSpin) with the following parameter values: effective TE, 4.0 ms; TR, 8.0 ms; flip angle, 15°; average number, 15; acquisition matrix, 256 × 256 × 128; FOV, 25.6 × 25.6 × 12.8 mm; total scan time, 38 minutes, 24 seconds. The resulted resolution was 100 μm/pixel. For determination of axial length, the digitized 3D images were analyzed using Osirix software (version 3.9.4) (5). First, the virtual horizontal plane through the optic nerve entry point was set. Then, the virtual vertical plane through and the optical axis were obtained. Axial lengths were manually determined in the images by a researcher blinded to genotype. Means of left and right eye axial lengths were first calculated for each animal. The mean values for each animal were used to determine the mean and SE for each genotype group (WT, $n = 13$; *Slitrk6* KO, $n = 10$). Statistical analysis was performed using 2-tailed Student's *t* test.

Histological analysis. All histological analyses were performed after mice were deeply anesthetized and killed by ether inhalation. For axial length determination in newborn mice, heads were rapidly frozen on dry ice and serially sectioned in horizontal planes at a thickness of 20 μm. After immersing in 4% paraformaldehyde plus 0.1 M sodium phosphate (pH 7.4) for 20 minutes at room temperature (RT), the sections were stained with hematoxylin and eosin. For all sections, the digitized images were obtained by NDP slide scanner (Hamamatsu Photonics). Images were manually aligned using Free-D software (6), and the axial length was calculated from the x, y, and z coordinates of the retinal internal surface of the optic nerve entry point and the anterior pole, which was determined as the center of the external surface of cornea with largest diameter among a series of sections.

In situ hybridization analysis was performed both on fresh-frozen post-fixed tissue sections as above and on frozen sections of the tissue that was fixed with 4% paraformaldehyde immersion (1 hour at RT) before freezing. The former sections (images in Figure 4) were better than the latter in terms of signal strength and morphology at low magnification. The procedure for the in situ hybridization was previously described (3). Digitized images were color-range-selected and contrast-brightness-optimized using Canvas X software (ACD Systems).

For immunofluorescence staining of retina, eyes at P7, P10, and adult stage were dissected out, fixed by 4% paraformaldehyde immersion for 1 hour, cryoprotected in 20% sucrose plus PBS for 3 hours, and frozen in OCT compound (Sakura Finetechnical). Adult eyes were freshly frozen, sectioned, and 4% paraformaldehyde immersion–fixed for 20 minutes at RT. The sections (10 μm) were rinsed with PBS and immersed in a blocking buffer consisting of 2% normal goat serum, 0.1% Triton X-100, and PBS for 1 hour at RT. The first antibody (rabbit anti-Ribeye polyclonal, 1:500, Synaptic Systems; guinea pig anti-Vglut1 polyclonal, 1:1,000, Millipore; rabbit anti-Vgat polyclonal, 1:800, Synaptic Systems; rat anti-synaptophysin monoclonal, 1:100, Sigma-Aldrich; mouse anti-neurofilament 160 monoclonal, 1:200, NN18, Sigma-Aldrich; mouse anti–βIII tubulin monoclonal, 1:1,000, Promega; rabbit anti-rhodopsin polyclonal, 1:200, Cosmo Bio; rat anti-Thy1 [CD90.2] monoclonal, 1:200, BD Biosciences; mouse anti–protein kinase C α monoclonal, 1:400, Sigma-Aldrich; rabbit anti–tyrosine hydroxylase polyclonal, 1:400, Chemicon; mouse anti–glutamine synthase monoclonal, 1:500, Chemicon) was diluted with blocking buffer and applied to the sections overnight at 4°C. After PBS wash (10 minutes, 3×), sections were incubated with secondary antibody (anti-rabbit IgG and anti-guinea pig IgG coupled with either Alexa Fluor 488 or Alexa Fluor 594, 1:500 each, Jackson ImmunoResearch Labs) at RT for 30 minutes, washed with PBS, and mounted with Vectashield mounting medium with DAPI (Vector Labs). Confocal images were taken with an Olympus FV1000 microscope and quantitatively analyzed using ImageJ software. Densitometric values of immunofluorescence signals were determined in comparable regions of retina from right eyes. Mean values of 2 independent images were analyzed for each mouse and used to determine mean and SE for each genotype group (WT, n = 12 or 13; *Slitrk6* KO, n = 17 or 18).

Statistics. Parametric data were analyzed using 2-tailed Student's t test. Data are presented as mean ± SEM. Differences were considered statistically significant for P values less than 0.05.

Study approval. Human studies were approved by the Ethics Committees of Ankara University (Ankara, Turkey), South West London (London, United Kingdom), and the Institute of Child Health (Athens, Greece) and by the IRBs at the University of Miami (Miami, Florida, USA) and University of Arizona (Tucson, Arizona, USA). Informed consent was obtained from all participants, or, in the case of minors, from the parents. Diagnosis of sensorineural hearing loss was established via standard audiometry in a soundproofed room according to current clinical standards. Hearing loss was classified according to the GENDEAF guidelines from the Hereditary Hearing Loss Homepage (http://hereditaryhearingloss.org/). Clinical evaluation of affected individuals included a thorough physical examination. All subjects underwent complete ophthalmologic examinations, including visual acuity test, anterior segment evaluation, intraocular pressure measurement, and fundus examination as well as otoscopy, tandem walking, and Romberg tests.

All animal experiments were approved by the Animal Experiment Committee of the RIKEN Brain Science Institute (approval no. H18-2B032), and mice were maintained at the RIKEN BSI Research Resource Center.

Accession numbers. Data were deposited in GenBank (human *SLITRK6*, accession nos. NM_032229 and NP_115605; mouse *Slitrk6*, accession nos. NM_175499 and NP_780708). The targeted allele ID is MGI:4417931.

Acknowledgments

This work was supported by NIH grant R01DC009645 (to M. Tekin), Birth Defects Foundation (United Kingdom)/Newlife Foundation for Disabled Children, RIKEN BSI funds, Strategic Research Program of RIKEN, Research to Prevent Blindness, and a MEXT (Ministry of Education, Culture, Sports, Science, and Technology, Japan) Grant-in-Aid for Scientific Research (A) (21240031). We thank all families for participating in this study, Tatiana V. Tkatchenko for advice on MRI analysis, Hideto Takahashi and Jaewon Ko for helpful advice on synapse induction assay, and Research Resource Center RIKEN staff for assistance in antibody generation and animal maintenance. Illumina cytoSNP analysis and sequencing was carried out at the Medical Biomics Centre (SGUL).

Received for publication July 17, 2012, and accepted in revised form January 31, 2013.

Address correspondence to: Mustafa Tekin, Dr. John T. Macdonald Foundation, Department of Human Genetics, 1501 NW 10th Avenue, BRB-610 (M-860), Miami, Florida 33136, USA. Phone: 305.243.2381; Fax: 305.243.3919; E-mail: mtekin@med.miami.edu. Or to: Andrew Crosby, Centre for Genetics, St Georges University London, London SW17 0RE. Phone: 44.208.725.0229; Fax: 44.208 725.1039; E-mail: acrosby@sgul.ac.uk. Or to: Jun Aruga, Jun Aruga Laboratory, RIKEN Brain Science Institute, Wako, Saitama 351-0198, Japan. Phone: 81.48.467.9791; Fax: 81.48.467.9792; E-mail: jaruga@brain.riken.jp.

1. Wojciechowski R. Nature and nurture: the complex genetics of myopia and refractive error. *Clin Genet*. 2011;79(4):301–320.
2. Kempen JH, et al. The prevalence of refractive errors among adults in the United States, Western Europe, and Australia. *Arch Ophthalmol*. 2004;122(4):495–505.
3. Vitale S, Ellwein L, Cotch MF, Ferris FL, Sperduto R. Prevalence of refractive error in the United States, 1999–2004. *Arch Ophthalmol*. 2008;126(8):1111–1119.
4. Lin LL, Shih YF, Hsiao CK, Chen CJ. Prevalence of myopia in Taiwanese schoolchildren: 1983 to 2000. *Ann Acad Med Singapore*. 2004;33(1):27–33.
5. Fredrick DR. Myopia. *BMJ*. 2002;324(7347):1195–1199.
6. Ardle BM, Bitner-Glindzicz M. Investigation of the child with permanent hearing impairment. *Arch Dis Child Educ Pract Ed*. 2010;95(1):14–23.
7. Mutti DO, Mitchell GL, Moeschberger ML, Jones LA, Zadnik K. Parental myopia, near work, school achievement, and children's refractive error. *Invest Ophthalmol Vis Sci*. 2002;43(12):3633–3640.
8. Zadnik K, Satariano WA, Mutti DO, Sholtz RI, Adams AJ. The effect of parental history of myopia on children's eye size. *JAMA*. 1994;271(17):1323–1327.
9. Dirani M, et al. Heritability of refractive error and ocular biometrics: the Genes in Myopia (GEM) twin study. *Invest Ophthalmol Vis Sci*. 2006;47(11):4756–4761.
10. Hornbeak DM, Young TL. Myopia genetics: a review of current research and emerging trends. *Curr Opin Ophthalmol*. 2009;20(5):356–362.
11. Guggenheim JA, Kirov G, Hodson SA. The heritability of high myopia: a reanalysis of Goldschmidt's data. *J Med Genet*. 2000;37(3):227–231.
12. Shi Y, et al. Genetic variants at 13q12.12 are associated with high myopia in the Han Chinese population. *Am J Hum Genet*. 2011;88(6):805–813.
13. Hysi PG, et al. A genome-wide association study for myopia and refractive error identifies a susceptibility locus at 15q25. *Nat Genet*. 2010;42(10):902–905.
14. Solouki AM, et al. A genome-wide association study identifies a susceptibility locus for refractive errors and myopia at 15q14. *Nat Genet*. 2010;42(10):897–901.
15. Li YJ, et al. Genome-wide association studies reveal genetic variants in CTNND2 for high myopia in Singapore Chinese. *Ophthalmology*. 2011;118(2):368–375.
16. Mordechai S, et al. High myopia caused by a mutation in LEPREL1, encoding prolyl 3-hydroxylase 2. *Am J Hum Genet*. 2011;89(3):438–445.
17. Mafong DD, Pletcher SD, Hoyt C, Lalwani AK. Ocular findings in children with congenital sensorineural hearing loss. *Arch Otolaryngol Head Neck Surg*. 2002;128(11):1303–1306.
18. Robin NH, Moran RT, Warman M, Ala-Kokko L. Stickler Syndrome. In: Pagon RA, Bird TD, Dolan CR, Stephens K, Adam MP, ed. *GeneReviews*. Seattle, Washington, USA: University of Washington, Seattle; 2011.
19. Kantarci S, et al. Mutations in LRP2, which encodes the multiligand receptor megalin, cause Donnai-Barrow and facio-oculo-acoustico-renal syndromes. *Nat Genet*. 2007;39(8):957–959.
20. Aruga J, Yokota N, Mikoshiba K. Human SLITRK family genes: genomic organization and expression profiling in normal brain and brain tumor tissue. *Gene*. 2003;315:87–94.
21. Aruga J. Slitrk6 expression profile in the mouse embryo and its relationship to that of Nlrr3. *Gene Expr Patterns*. 2003;3(6):727–733.
22. Takahashi H, et al. Selective control of inhibitory synapse development by Slitrk3-PTPδ trans-synaptic interaction. *Nat Neurosci*. 2012;15(3):389–398.
23. Aruga J, Mikoshiba K. Identification and character-

ization of Slitrk, a novel neuronal transmembrane protein family controlling neurite outgrowth. *Mol Cell Neurosci*. 2003;24(1):117–129.

24. Katayama K, et al. Disorganized innervation and neuronal loss in the inner ear of Slitrk6-deficient mice. *PLoS One*. 2009;4(11):e7786.
25. Matsumoto Y, et al. Impaired auditory-vestibular functions and behavioral abnormalities of Slitrk6-deficient mice. *PLoS One*. 2011;6(1):e16497.
26. Tkatchenko TV, Shen Y, Tkatchenko AV. Analysis of postnatal eye development in the mouse with high-resolution small animal magnetic resonance imaging. *Invest Ophthalmol Vis Sci*. 2010;51(1):21–27.
27. Meng W, Butterworth J, Malecaze F, Calvas P. Axial length of myopia: a review of current research. *Ophthalmologica*. 2011;225(3):127–134.
28. Sterling P, Matthews G. Structure and function of ribbon synapses. *Trends Neurosci*. 2005;28(1):20–29.
29. Proenca CC, Gao KP, Shmelkov SV, Rafii S, Lee FS. Slitrks as emerging candidate genes involved in neuropsychiatric disorders. *Trends Neurosci*. 2011;34(3):143–153.
30. Beaubien F, Cloutier JF. Differential expression of Slitrk family members in the mouse nervous system. *Dev Dyn*. 2009;238(12):3285–3296.
31. Wallman J, Winawer J. Homeostasis of eye growth and the question of myopia. *Neuron*. 2004;43(4):447–468.
32. Mutti DO, et al. Axial growth and changes in lenticular and corneal power during emmetropization in infants. *Invest Ophthalmol Vis Sci*. 2005;46(9):3074–3080.
33. Norton TT. Animal models of myopia: learning how vision controls the size of the eye. *ILAR J*. 1999;40(2):59–77.
34. Seki M, Nawa H, Fukuchi T, Abe H, Takei N. BDNF is upregulated by postnatal development and visual experience: quantitative and immunohistochemical analyses of BDNF in the rat retina. *Invest Ophthalmol Vis Sci*. 2003;44(7):3211–3218.
35. Sirmaci A, Edwards YJ, Akay H, Tekin M. Challenges in whole exome sequencing: an example from hereditary deafness. *PLoS One*. 2012;7(2):e32000.
36. Li H, Durbin R. Fast and accurate long-read alignment with Burrows-Wheeler transform. *Bioinformatics*. 2010;26(5):589–595.
37. McKenna A, et al. The Genome Analysis Toolkit: a MapReduce framework for analyzing next-generation DNA sequencing data. *Genome Res*. 2010;20(9):1297–1303.
38. DePristo MA, et al. A framework for variation discovery and genotyping using next-generation DNA sequencing data. *Nat Genet*. 2011;43(5):491–498.
39. Inoue T, Ota M, Ogawa M, Mikoshiba K, Aruga J. Zic1 and Zic3 regulate medial forebrain development through expansion of neuronal progenitors. *J Neurosci*. 2007;27(20):5461–5473.